Chapter 4
X-Ray and Neutron Pair Distribution Function Analysis

Yohei Onodera, Tomoko Sato, and Shinji Kohara

Abstract Pair distribution function (PDF) obtained by X-ray diffraction (XRD) and neutron diffraction (ND) measurements enables us to probe the structure of disordered materials, which has no long-range order and periodicity. This chapter provides an introduction to PDF analysis using XRD and ND techniques. A brief outline of the theory of diffraction for disordered materials is given with a focus on the use of various real-space functions. The structures of single-component disordered materials are introduced to understand the origins of characteristic diffraction peaks, i.e., the first sharp diffraction peak (FSDP) and the principal peak (PP), observed in broad halo patterns. Furthermore, the instrumentation of synchrotron X-rays and neutrons for PDF analysis with associated results for the structural studies of disordered materials under high temperature and high pressure are reviewed.

Keywords X-ray diffraction · Neutron diffraction · Pair distribution function · Glass · Structure

Y. Onodera
Institute for Integrated Radiation and Nuclear Science, Kyoto University, Osaka 590-0494, Japan
e-mail: y-onodera@rri.kyoto-u.ac.jp

T. Sato
Department of Earth and Planetary Systems Science, Hiroshima University, Hiroshima 739-8526, Japan
e-mail: tomokos@hiroshima-u.ac.jp

S. Kohara (✉)
Research Center for Advanced Measurement and Characterization, National Institute for Materials Science, Ibaraki 305-0047, Japan
e-mail: KOHARA.Shinji@nims.go.jp

K. Hayashi (ed.), *Hyperordered Structures in Materials*, The Materials Research Society Series, https://doi.org/10.1007/978-981-99-5235-9_4

4.1 Introduction

The complementary use of different quantum beam diffraction (X-ray diffraction (XRD) and neutron diffraction (ND)) measurements, such as synchrotron X-ray, neutron, and electron diffraction measurements, is quite useful in investigating the atomistic structure of functional materials. In the case of crystalline materials, their crystal structure can be determined on the basis of crystallography, which focuses on the symmetry and periodicity of the atomic arrangement in crystalline materials, with the aid of diffraction measurements. On the other hand, the structure of disordered materials, e.g., liquid, glassy, and amorphous solids, has no distinct translational symmetry and periodicity, and therefore cannot be analyzed on the basis of crystallography. Therefore, the measurement of pair distribution function (PDF) using different quantum beam diffraction techniques is a canonical approach to probing atomic arrangements in disordered materials. The PDF expresses the probability of finding atomic pairs separated by a certain distance, which provides us with the real-space information on the structure of disordered materials. Furthermore, PDF analysis has recently been used to examine the local structural disorder in crystalline materials. In this chapter, a brief introduction to PDF analysis using XRD and ND is given. First, the basic theory of diffraction experiments is described. Next, the structures of single-component oxide glasses, such as silica (SiO_2) glass are reviewed to understand the origins of diffraction peaks in broad halo patterns. Moreover, the structure and diffraction data of oxide liquids and glasses under high temperatures and high pressures are introduced.

4.2 Diffraction Theory

In PDF analysis, diffraction patterns can be considered as a function of Q, which gives the magnitude of the scattering vector given by

$$Q = \frac{4\pi \sin\theta}{\lambda}, \tag{4.1}$$

where 2θ is the scattering angle and λ is the incident wavelength of X-rays or neutrons. The scattering intensity of materials containing n chemical species is normalized to give the total structure factor, $S(Q)$ [1, 2],

$$S(Q) = 1 + \frac{1}{|\langle W(Q)\rangle|^2} \sum_{\alpha=1}^{n} \sum_{\beta=1}^{n} c_\alpha c_\beta w_\alpha^*(Q) w_\beta(Q) \big[S_{\alpha\beta}(Q) - 1\big], \tag{4.2}$$

where c_α is the atomic fraction of chemical species α and $w_\alpha(Q)$ is either a Q-independent coherent scattering length in ND or Q-dependent atomic scattering (form) factor with dispersion terms in XRD. $S_{\alpha\beta}(Q)$ is a partial structure factor

and

$$\langle W(Q)\rangle = \sum_{\alpha} c_{\alpha} w_{\alpha}(Q). \tag{4.3}$$

Since X-rays are scattered by electron clouds in atoms, the X-ray atomic form factor depends on the atomic number. On the other hand, neutrons are scattered by their interactions with atomic nuclei, and the neutron coherent scattering length varies independent of the atomic number. In other words, X-rays are sensitive to heavy elements whereas neutrons are sensitive to light elements. Therefore, the complementary use of XRD and ND is robust for revealing the atomic arrangements in materials containing several chemical species.

The corresponding structural information in real space is contained in the PDF $g(r)$ obtained by a Fourier transform of $S(Q)$,

$$g(r) = 1 + \frac{1}{2\pi^2 r\rho} \int_{Q_{\min}}^{Q_{\max}} Q(S(Q) - 1)\sin(Qr)M(Q)dQ, \tag{4.4}$$

where r is the interatomic distance, ρ is the atomic number density in Å^{-3}, and $M(Q)$ is the Lorch [3] modification function, $M(Q) = \sin(\pi Q/Q_{\max})/(\pi Q/Q_{\max})$ for $Q \leqq Q_{\max}$, and $M(Q) = 0$ for $Q > Q_{\max}$ where $Q_{\max}$ is the maximum value of Q. To obtain structural information with a sufficient real-space resolution, it is indispensable to obtain $S(Q)$ up to the high-Q region because a high real-space resolution is achieved by a Fourier transform of $S(Q)$ with a large $Q_{\max}$ [4]. The structure of a material containing n chemical species is given by $n(n + 1)/2$ of these partial PDFs.

The reduced PDF $G(r)$ is derived from a Fourier transform of $S(Q)$ as follows.

$$G(r) = \frac{2}{\pi} \int_{Q_{\min}}^{Q_{\max}} Q(S(Q) - 1)\sin(Qr)M(Q)dQ. \tag{4.5}$$

The PDF $g(r)$ is derived from the following equation.

$$g(r) = \frac{G(r)}{4\pi r\rho} + 1. \tag{4.6}$$

The total correlation function $T(r)$ and the radial distribution function $RDF(r)$ are obtained from the following equations:

$$T(r) = G(r) + 4\pi r\rho = 4\pi r\rho g(r), \tag{4.7}$$

$$RDF(r) = rG(r) + 4\pi r^2\rho = 4\pi r^2\rho g(r) = rT(r). \tag{4.8}$$

The coordination number of type β atoms around a type α atom, $N_{\alpha\beta}$, which is the number of atoms of type β between r_1 and r_2 ($r_1 < r_2$) from an atom of type α, is calculated from the partial radial distribution functions $RDF_{\alpha\beta}(r)$ as

$$N_{\alpha\beta} = \int_{r_1}^{r_2} RDF_{\alpha\beta}(r)\mathrm{d}r = \int_{r_1}^{r_2} 4\pi r^2 c_\beta \rho g_{\alpha\beta}(r)\mathrm{d}r. \tag{4.9}$$

Therefore, it is possible to obtain the coordination number when individual peaks, which arise from one partial radial distribution function, are assigned and extracted from $RDF(r)$. $T(r)$ is commonly used to analyze the atomic arrangement in oxide glasses. The reason for choosing $T(r)$, which scales as r, rather than other functions such as $g(r)$, which scales as a constant, and $RDF(r)$, which scales as r^2, is that it is broadened by thermal vibration [5]. Thus, $T(r)$ is more suitable for peak fitting than $g(r)$ [6]. By using the real-space functions mentioned above, we can obtain interatomic distances and coordination numbers of materials.

4.3 PDF Diffractometers at Advanced Quantum Beam Facilities

The advanced instrumentations at neutron and synchrotron facilities provide diffraction data in a wide Q range, which is achieved by using short-wavelength (high-energy) neutrons and X-rays, thereby providing diffraction data in a wide Q range [4]. High-energy X-ray PDF diffractometers are available at several synchrotron facilities, e.g., BL04B2 and BL08W at SPring-8, Japan [7], I15-1 at Diamond Light Source, UK [8], and 11-ID-C at the Advanced Photon Source, USA [9]. In the case of neuron diffractometers, D4 at the Institut Laue–Langevin, France [10], NOMAD at Spallation Neutron Source, USA [11], GEM and NIMROD at ISIS Neutron Source, UK [12], and NOVA at J-PARC, Japan [13] are available for PDF analysis of disordered materials.

4.4 GeO_2 Crystal and Glass

Figure 4.1a shows the X-ray $S(Q)$ of a GeO_2 crystal and glass [14] obtained by synchrotron XRD measurements. Germanium dioxide (GeO_2) is a prototypical glass-forming material and shares the same local structural motif as its crystalline counterpart. The germanium–oxygen coordination number is 4, suggesting that a tetrahedral corner-sharing network is formed. Although the $S(Q)$ of the GeO_2 crystal shows Bragg peaks that reflect its long-range periodicity, the $S(Q)$ of the GeO_2 glass shows a broad halo pattern owing to the lack of periodicity. The $T(r)$ are shown in

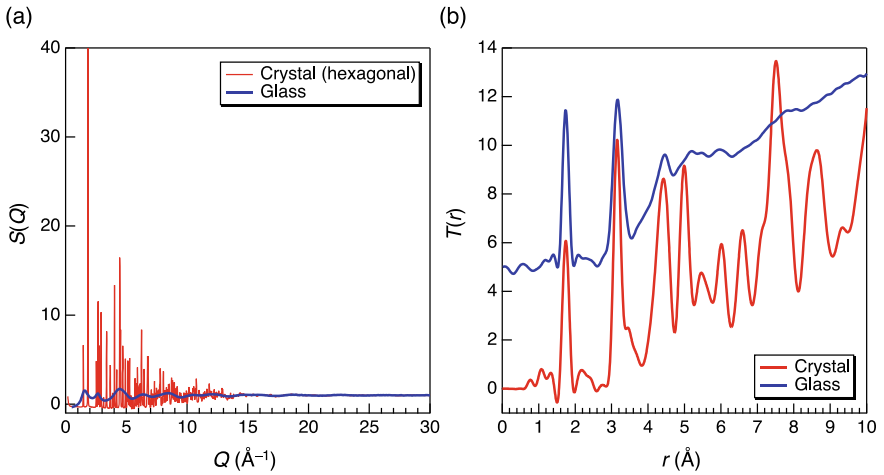

Fig. 4.1 **a** X-ray total structure factors $S(Q)$ and **b** total correlation functions $T(r)$ of GeO_2 crystal and glass

Fig. 4.1b. In $T(r)$ data of both the GeO_2 crystal and glass, Ge–O correlation peak is clearly observed at 1.74 Å since the GeO_4 tetrahedron is the shared structural motif in crystalline and glassy GeO_2. On the other hand, the Ge–Ge correlation peak, which corresponds to the distance between centers of corner-sharing GeO_4 tetrahedra, is observed at ~3.2 Å and is obviously diminished in the $T(r)$ for GeO_2 glass, indicating that the structure of GeO_2 glass is disordered in a length scale larger than the first cation–cation correlation length. Moreover, it is difficult to assign a peak beyond 4 Å in $T(r)$ to an atomic pair correlation for GeO_2 glass. To investigate the length scale beyond the nearest-neighbor correlation length, "intermediate-range order," structure modeling is an effective tool (see Chap. 10 for more information).

4.5 SiO_2 Glass

Silicon dioxide (SiO_2) is classified into a glass-forming material along with GeO_2, and it has a network structure in which the interconnections of SiO_4 tetrahedral motifs form a network by the corner sharing of oxygen atoms. Figure 4.2a shows the X-ray [7] and neutron [15] structure factors $S(Q)$ for SiO_2 glass. The first sharp diffraction peak (FSDP) [16, 17] appears at $Q \sim 1.5$ Å^{-1} in both X-ray and neutron $S(Q)$s, whereas the principal peak (PP) appears at $Q \sim 3$ Å^{-1} in only the neutron $S(Q)$ because the PP is correlated with the packing of oxygen atoms in oxide glasses [18]. By using Eq. (4.2), we calculate the weighting factors in the X-ray and neutron $S(Q)$ for SiO_2 glass as follows:

$$\text{X-ray}\, S(Q) = 0.218 S_{\text{Si–Si}}(Q) + 0.498 S_{\text{Si–O}}(Q) + 0.284 S_{\text{O–O}}(Q), \qquad (4.10)$$

$$\text{Neutron}\, S(Q) = 0.069 S_{\text{Si-Si}}(Q) + 0.388 S_{\text{Si-O}}(Q) + 0.543 S_{\text{O-O}}(Q), \quad (4.11)$$

where the Q-dependent atomic form factors are approximated using atomic numbers. As can be seen in the weighting factors calculated above, the weighting factor of the O–O correlation is large in the neutron $S(Q)$ compared with that in the X-ray $S(Q)$. Indeed, the X-ray- and neutron-weighted partial structure factors $S_{\alpha\beta}(Q)$ obtained by a combination of classical molecular dynamics (MD) simulation and reverse Monte Carlo (RMC) [19, 20] modeling indicate that the FSDP is observed owing to the positive contributions of $S_{\text{Si-Si}}(Q)$, $S_{\text{Si-O}}(Q)$, and $S_{\text{O-O}}(Q)$ in both the X-ray and neutron $S(Q)$s, whereas the positive Si–Si and O–O PPs are canceled out by the negative Si–O PP of the X-ray $S(Q)$ [19, 20]. Therefore, PP is visible in only ND data for oxide glasses, because the oxygen–oxygen correlation is dominant owing to its large weighting factor for ND. The FSDP was first discussed by Wright and Leadbetter in 1976 [21], although it seems that the term "FSDP" was first used by Phillips in 1981 [22]. It is common knowledge that the FSDP of SiO_2 glass is associated with the continuous random network model proposed by Zachariasen [23], and the origin of the FSDP of SiO_2 glass has long been discussed [22, 24]. Onodera et al. have reported in 2019 that the FSDP in SiO_2 glass originates from the arrangement of tetrahedral SiO_4 motifs with the periodicity of 4 Å given by $2\pi/Q_{\text{FSDP}}$, where Q_{FSDP} is the position of the FSDP, with a coherence length of 10 Å given by $2\pi/\Delta Q_{\text{FSDP}}$ (ΔQ_{FSDP} is the full width at half-maximum of the FSDP) [19]. The $T(r)$ of SiO_2 glass is shown in Fig. 4.2b. In $T(r)$ data of both the X-ray and neutron, the Si–O correlation peak is clearly observed at 1.62 Å and the Si–O coordination number is 4.0 ± 0.1. The O–O and Si–Si correlation peaks are observed at 2.63 and 3.08 Å, respectively. It is notable that a prominent O–O correlation peak is observed in neutron $T(r)$, whereas a clearer Si–Si correlation peak is observed in X-ray $T(r)$. This is because of the difference between the weighting factors in XRD and ND data as shown in Eqs. (4.10) and (4.11), suggesting that the complementary use of X-ray and neutron enables us to analyze the glass structure more precisely.

4.6 Other Single-Component Disordered Materials

Figure 4.3 shows total structure factors $S(Q)$ of glassy (g)-$Cu_{50}Zr_{50}$ [19], amorphous (a)-Si [25], g-$ZnCl_2$ [26], g-$GeSe_2$ [27], g-GeS_2 [28], g-GeO_2 [29], g-SiO_2 [15], liquid (l)-CCl_4 [30], and l-P [31]. Note that Q is scaled by the nearest-neighbor distance d appearing in the $T(r)$ to eliminate the atomic size differences. The average metal–metal coordination number in g-$Cu_{50}Zr_{50}$ is approximately 12 and the local structural unit of g-$Cu_{50}Zr_{50}$ can be regarded as an icosahedron. The structural unit of other materials is a regular tetrahedron, although a-Si and all g-AX_2 materials have a network structure, whereas the two molecular liquids in which CCl_4 and P_4 tetrahedra are isolated do not form a network structure. In Fig. 4.3, three peaks, Q_1 (FSDP), Q_2 (PP), and Q_3, can be observed in the $S(Q)$ for all materials except for a-Si

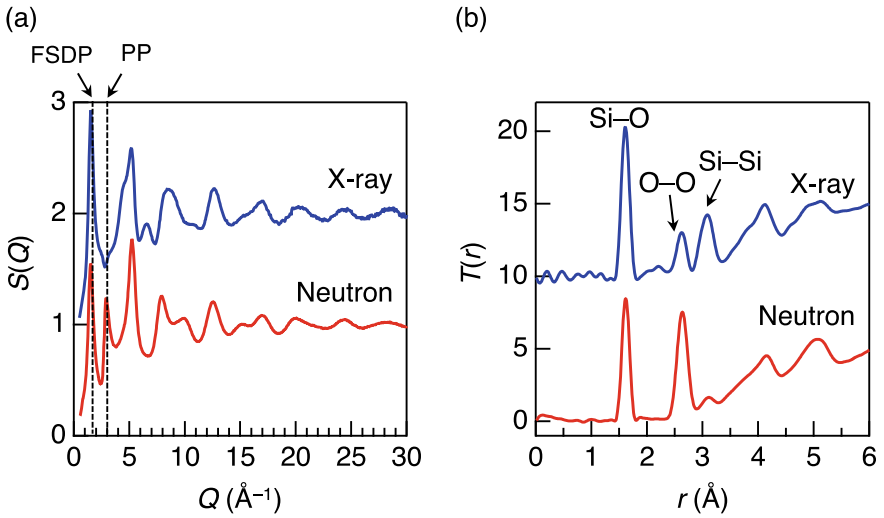

Fig. 4.2 **a** X-ray and neutron total structure factors $S(Q)$ and **b** total correlation functions $T(r)$ of SiO_2 glass

and g-$Cu_{50}Zr_{50}$, whereas the split of PP is observed in the $S(Q)$ for molecular liquids. Both g-$ZnCl_2$ [26] and g-$GeSe_2$ [27] have a small fraction of edge-sharing tetrahedra as well as corner-sharing ones. However, the three (Q_1, Q_2, Q_3)-peak structure seems to arise from mostly corner-sharing tetrahedra because the ratio of edge-sharing to corner-sharing tatrahedra is very small [26, 27]. The FSDP of g-GeO_2 observed at a larger Qd value stems from the structure with the higher packing of atoms in g-GeO_2 [32, 33]. Although the FSDP is observed in oxide glasses with a corner-sharing polyhedral network, it also appears in the $S(Q)$ of l-CCl_4 [30], l-P [31] (Fig. 4.3), and l-KPb [34–36] and other molecular liquids [37]. Thus, it is suggested that the FSDP is not a signature of a network formation. A prominent FSDP has appeared in the diffraction patterns of other network-forming materials, such as g-B_2O_3 [38] and g-As_2O_3 [39], but not in a-Si and a-Se [40]. Therefore, it can be concluded that the FSDP is a signature of a sparse distribution of planes in polyhedra, because the FSDPs of g-SiO_2 [41, 42] and l-P [31] diminish with the reduction of cavity volumes associated with the increase in pressure.

The origin of the PP is obvious in oxide glasses because the PP is correlated with the packing of oxygen atoms (at the corner of polyhedral units) [18]. For instance, the PP of the neutron $S(Q)$ of g-SiO_2 becomes sharper under high pressure [42]. On the other hand, the PP of the neutron $S(Q)$ of l-CCl_4 shown in Fig. 4.3 is split, which indicates the presence of intermolecular orientational correlations of CCl_4 tetrahedral motifs [37, 43, 44]. The orientational correlations appear in l-P and presumably in g-As_2O_3 [39] because their $S(Q)$ shows a split PP. Therefore, it seems that the PP reflects inter-polyhedral correlations observed in a small-length scale compared with FSDP in disordered materials. It is notable that the transition from a low-density

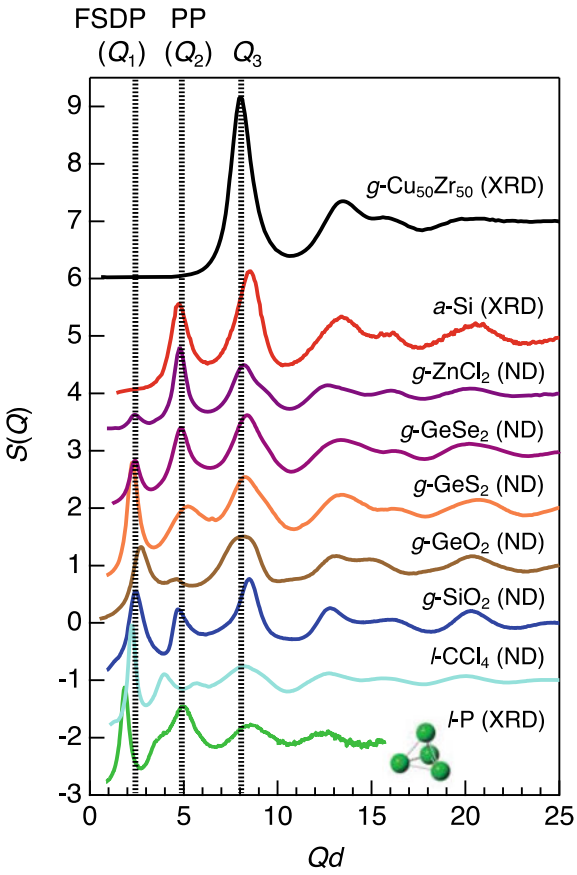

Fig. 4.3 Total structure factors $S(Q)$ of g-$Cu_{50}Zr_{50}$ [19], a-Si [25], g-$ZnCl_2$ [26], g-$GeSe_2$ [27], g-GeS_2 [28], g-GeO_2 [29], g-SiO_2 [15], l-CCl_4 [30], and l-P [31]. Scaling to the magnitude of scattering vector Q is applied by multiplying Q by d (first interatomic distance observed in total correlation functions). In the case of l-P, d is calculated on the basis of the side length of a P_4 tetrahedron

molecular liquid to a high-density network in l-P under extreme conditions leads to the diminishment of FSDP. On the other hand, a remarkable FSDP appears in the X-ray $S(Q)$ of the low-density molecular l-P (Fig. 4.3). This result implies that the FSDP also appears in the arrangement of tetrahedra without the central atom, because the $S(Q)$ of molecular l-P shows the remarkable FSDP even though a P_4 tetrahedron does not contain a central atom as shown in Fig. 4.3. Only Q_3 is found in X-ray $S(Q)$ of g-$Cu_{50}Zr_{50}$, which has a dense random packing (DRP) structure [45–47]. Therefore, the local structure of g-$Cu_{50}Zr_{50}$ is markedly different from a tetrahedral structure owing to the absence of a strong chemical bond, indicating that the PP is a signature of the formation of a chemical bond because g-$Cu_{50}Zr_{50}$ has no strong chemical bond owing to its DRP structure.

Kohara et al. have compared the atomic structure of liquid and solidified (crystalline and amorphous) Si with those of SiO_2 [48]. Although the short-range structural unit is a regular tetrahedron in a-Si and g-SiO_2, the chemical contrast (Si is fourfold and O is twofold) in the SiO_4 unit in g-SiO_2 is not found in the $SiSi_4$ unit because the number of all atoms is fourfold in a-Si. Figure 4.4a shows the X-ray $S(Q)$ of

a-Si [25] together with that of *l*-Si (1770 K) [19]. In the X-ray $S(Q)$ of *a*-Si, prominent Q_2 (PP) and Q_3 are observed at $Qr_{A-X} \sim 5$ and 8.5, respectively, although no Q_1 (FSDP) is observed. However, the $S(Q)$ of *l*-Si is markedly different from that of *a*-Si, as shown in Fig. 4.4a. This is because of the large difference in the Si–Si coordination number N_{Si-Si}, 3.9 in amorphous solid [25] versus 5.7 in liquid [19], associated with the remarkable increase in density from 2.30 g/cm^3 in amorphous solid to 2.57 g/cm^3 in liquid. Figure 4.4b shows the X-ray [7] and neutron [15] $S(Q)$ of *g*-SiO_2 together with the X-ray $S(Q)$ of *l*-SiO_2 (2019 K) [49]. Note that the X-ray $S(Q)$ of *l*-SiO_2 is comparable to that of *g*-SiO_2. A sharp FSDP is observed in both the $S(Q)$s of *l*/*g*-SiO_2, indicating that strong Si–O covalent bonds are maintained even in *l*-SiO_2. These behaviors are consistent with the small differences in the Si–O coordination number N_{Si-O} (4.0 in glass and 3.9 in liquid) and density (2.20 g/cm^3 in glass and 2.10 g/cm^3 in liquid) between glass and liquid. Furthermore, Kohara et al. revealed the difference between *a*-Si and *g*-SiO_2 in terms of the network topology revealed by quantum beam diffraction measurements, structure modeling based on diffraction data, and a series of topological analyses. They showed that the narrower ring size distribution and the smaller cavity volume ratio in *a*-Si than in *g*-SiO_2 is a signature of an extremely poor amorphous-forming ability of *a*-Si [48]. Moreover, they concluded that the chemical contrast in the corner-sharing tetrahedral network in AX_2 (A, fourfold cation; X, twofold anion) is crucial for good amorphous-forming ability [48].

4.7 Al_2O_3 Glass (Single-Component Intermediate Oxide Glass)

The basic concept for the formation of glass is the tetrahedral motif with corner-sharing oxygen atoms proposed by Zachariasen in 1932. In Zachariasen's rule, the coordination number of oxygen atoms (n) around a cation (A) is limited to 3–4 and AO_n polyhedra form a corner-sharing network [23]. Fifteen years after Zachariasen's proposal, Sun reported the classification of single-component oxides into glass formers, glass modifiers, and intermediates [50] (The details of the classification proposed by Sun are discussed in Chap. 15). Alumina (Al_2O_3) is classified into an intermediate. Al_2O_3 acts as a glass former and a glass modifier in binary oxide glasses, although Al_2O_3 cannot sorely form glass via a melt-quenching approach. Hashimoto et al. reported that electrochemically synthesized amorphous Al_2O_3 shows a glass transition, demonstrating that Al_2O_3 is a glass (*g*-Al_2O_3) [51]. The density of *g*-Al_2O_3 measured using a gas pycnometer is 3.05 g/cm^3, which is smaller than those for crystalline Al_2O_3 (α-Al_2O_3, 4.00 g/cm^3; γ-Al_2O_3, 3.59 g/cm^3) and slightly larger than that for *l*-Al_2O_3 (2.92 g/cm^3) [52]. Figure 4.5 shows the X-ray and neutron total structure factors $S(Q)$ of *g*-Al_2O_3, *g*-SiO_2 [7, 15], and *l*-Al_2O_3 (2400 K) [52]. The FSDP, which originates from a sparse distribution of planes in polyhedra, is clearly observed at $Q = 1.52$ Å^{-1} in the $S(Q)$ of *g*-SiO_2, whereas the FSDP observed at

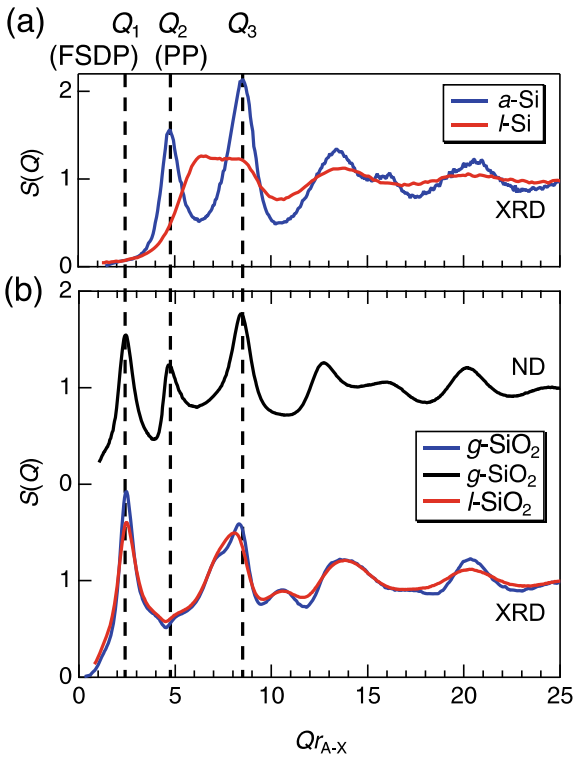

Fig. 4.4 **a** X-ray total structure factors $S(Q)$ of *a*-Si [25] and *l*-Si (1770 K) [19]. **b** X-ray total structure factors $S(Q)$ of *g*-SiO_2 [7] and *l*-SiO_2 (2019 K) [49], together with neutron $S(Q)$ [15] of *g*-SiO_2. Scaling to the magnitude of scattering vector Q is applied by multiplying Q by $r_{A–X}$ (first interatomic distance observed in total correlation functions). Taken from Ref. [48]

$Q \sim 2$ Å^{-1} is not sharp in the $S(Q)$ of *g*-Al_2O_3, suggesting that the absence of the corner-sharing polyhedral motif with a large cavity volume, which is a signature in typical glass formers. The neutron $S(Q)$ of *g*-Al_2O_3 shows an extraordinarily sharp PP, whereas the X-ray $S(Q)$ of *g*-Al_2O_3 shows no PP owing to the small O–O weighting factor. Since PP is an indicator of the packing of oxygen atoms, the extraordinarily sharp PP in the neutron $S(Q)$ indicates that a structure with densely packed oxygen atoms is formed in *g*-Al_2O_3. The neutron $S(Q)$ of *l*-Al_2O_3 is broader than that of *g*-Al_2O_3 especially in the PP, whereas the X-ray $S(Q)$ of *l*-Al_2O_3 and *g*-Al_2O_3 are more identical, indicating that oxygen-related structure is different between *l*-Al_2O_3 and *g*-Al_2O_3.

Figure 4.6 shows the X-ray and neutron total correlation functions $T(r)$ of *g*-Al_2O_3 [51], *l*-Al_2O_3 [52], and *g*-SiO_2 [7, 15]. The first peak of the $T(r)$ of *g*-Al_2O_3 observed at 1.81 Å is assigned to the Al–O correlations. The second peak observed at 2.8 Å in the neutron $T(r)$ and that observed at 3.2 Å in X-ray $T(r)$ are assigned to O–O and Al–Al correlations, respectively. The Al–O atomic distance in *g*-Al_2O_3 is longer than the Si–O atomic distance in *g*-SiO_2. In addition, the Al–O correlation peak shows an asymmetric shape with a tail of ~2.4 Å. These results suggest that distorted AlO_n polyhedra are formed with an Al–O coordination number $N_{Al–O}$ greater than 4. Indeed, the $N_{Al–O}$ is found to be 4.6 ± 0.2, which is identical to the results of

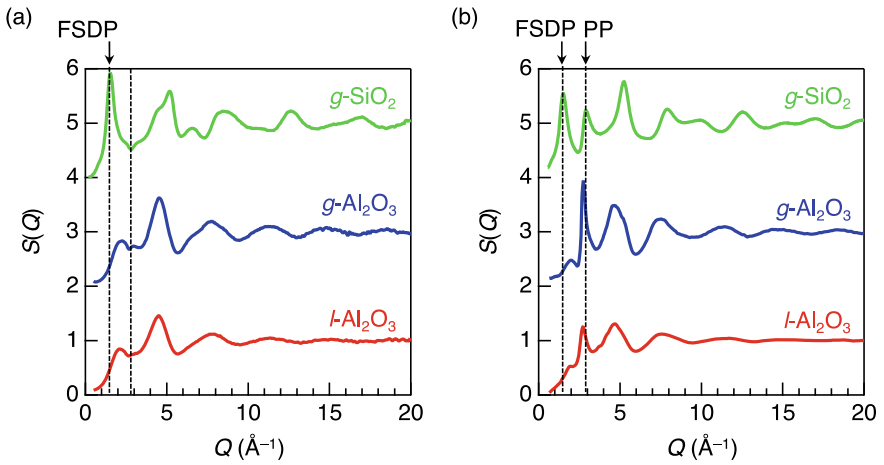

Fig. 4.5 **a** X-ray and **b** neutron total structure factors $S(Q)$ of g-Al_2O_3 (2400 K) [51], l-Al_2O_3 [52], and g-SiO_2 [7, 15]

NMR measurements ($N_{Al–O} = 4.73$) and higher than 4.4 in l-Al_2O_3 (2400 K) [52]. Such a high cation–oxygen coordination number, which is frequently observed in high-temperature nonglass-forming oxide liquids [53, 54], can hardly be observed in the typical glass formers and glass-forming liquids.

Hashimoto et al. also performed MD-RMC modeling to reveal the structure of g-Al_2O_3. The MD-RMC model suggests that OAl_3 triclusters are formed by the edge-sharing AlO_n polyhedra ($n = 4$–6). In addition, they reported that the edge-sharing

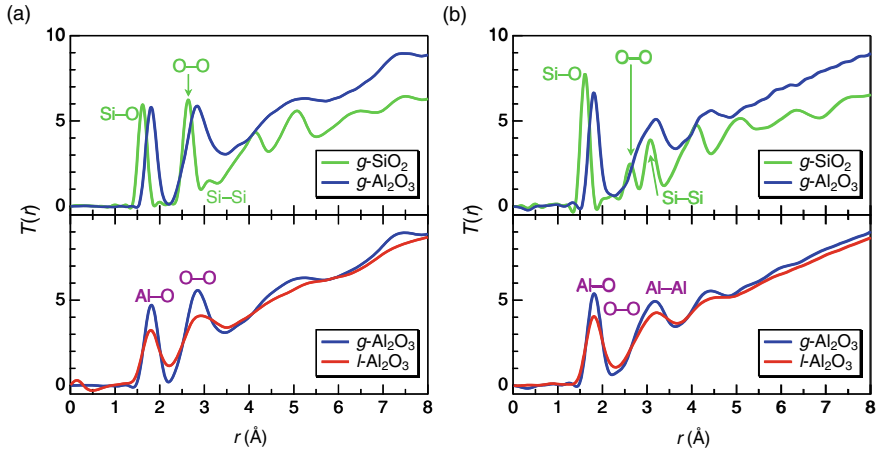

Fig. 4.6 **a** X-ray and **b** neutron total correlation functions $T(r)$ of g-Al_2O_3 [51], l-Al_2O_3 (2400 K) [52], and g-SiO_2 [7, 15]. Upper- and lower-panel data were obtained by Fourier transforms of $S(Q)$ with $Q_{max} = 25$ and 18 Å^{-1}, respectively

AlO_n polyhedra forms a lattice-like structure with an O–O distance of ~2.3–2.7 Å. This distance is nearly identical to the periodicity of ~2.3 Å calculated from the peak position of the PP observed in the neutron $S(Q)$ of g-Al_2O_3. Therefore, they concluded that the formation of large amounts of AlO_5 and AlO_6 polyhedra, which is outside of Zachariasen's conventional glass-forming concept, might be the origin of the extraordinarily sharp PP in the neutron $S(Q)$ of g-Al_2O_3. The electrochemically synthesized g-Al_2O_3, which is the first successfully synthesized single-component intermediate glass, has many features, such as the densely oxygen-packed structure with a large fraction of edge-sharing polyhedra, that is completely outside of the conventional glass-forming concept [51]. Controlling the formation of a unique structure will provide glass with novel characteristics, e.g., hardness, crack resistance, and permittivity. Therefore, the fabrication of intermediate oxide glasses via an electrochemical approach is a useful tool for creating new glass materials.

4.8 Diffraction Measurements Under High Temperature

Understanding the structure of high-temperature liquids provides us with useful information for understanding the nature of glass transition. However, the clarification of atomic arrangements in high-temperature liquid is a challenging scientific task, because chemical reactions of liquids with sample containers are very difficult to avoid. Moreover, the Bragg peaks from a crystalline container disturb the measurement of high-quality diffraction data from liquids. To overcome these problems, several containerless levitation techniques have been developed [55]. The details of various levitation techniques are described in Chap. 7. Levitation techniques also enable the access of deep undercooled liquids and enhance glass formation because heterogeneous nucleation is avoided (glass preparations using a levitation technique are discussed in Chap. 15). The structure of a typical nonglass-forming liquid, l-Al_2O_3, has been investigated by XRD, ND, and MD simulations [52, 55–61]. Furthermore, structures of UO_2 [62] and the UO_2–ZrO_2 system [63], the common nuclear fuel component of a reactor, have been studied. The structures of ZrO_2 [53, 64, 65], HfO_2 [65], and Lanthanide oxides [54, 64] have been studied to clarify the physicochemical properties of high-temperature liquids. In this chapter, the dedicated high-energy X-ray diffractometer for diffraction measurements on levitated liquids is described. In addition, representative structural studies of high-temperature oxide liquids by a combination of levitation techniques and diffraction measurements are introduced.

The dedicated PDF diffractometer for liquid, glassy, and amorphous materials is developed at the high-energy XRD beamline BL04B2 of SPring-8. The details of the diffractometer are described in Refs. [7, 66]. The diffractometer has four CdTe detectors (low-scattering-angle regions) and three Ge detectors (high-scattering-angle regions, see Fig. 4.7a). The experimental setup for the XRD measurements on levitated liquids at the BL04B2 beamline with an aerodynamic levitator [4, 67] is shown in Fig. 4.7b. A sample of 2 mm diameter is levitated by dry air and heated

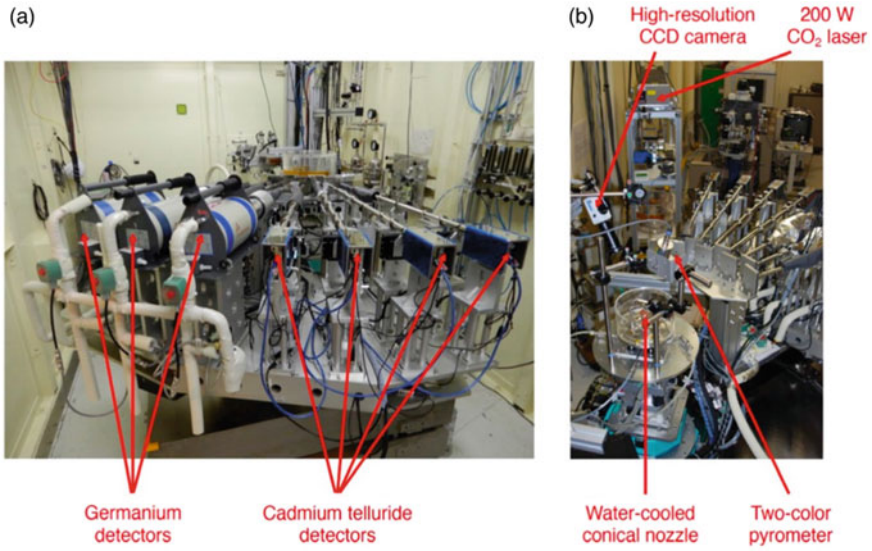

Fig. 4.7 **a** Dedicated high-energy X-ray PDF diffractometer installed at the BL04B2 of SPring-8. **b** Aerodynamic levitator [4] installed on the PDF diffractometer. Reproduced from Ref. [66] (CC BY 4.0)

by a CO_2 laser. The temperature of the levitated sample is measured by a pyrometer. Note that the use of a levitation technique eliminates the Bragg peaks originating from a crystalline container, realizing the measurements of high-quality diffraction data at high temperatures.

In addition to the basic concept of glass-forming materials proposed by Zachariasen [23] and Sun [50], Angell [68] proposed the concept of "fragility" in glass-forming liquids. He interpreted the behavior of strong and fragile liquids on the basis of topological differences. SiO_2, GeO_2, and B_2O_3 are classified into typical strong liquids. They have a covalently bonded cation–oxygen network, and their viscosities obey the Arrhenius law. In contrast, chalcogenide and iron phosphates are regarded as typical fragile liquids. Their networks are almost ionic, and their viscosities markedly deviate from the Arrhenius behavior. Determining the structure of oxide liquids under high temperatures is crucial for clarifying the fragility of liquids.

Er_2O_3, a representative nonglass former, has an exceedingly high melting temperature (T_m) of 2686 K. Koyama et al. reported the results of high-energy XRD and density measurements on l-Er_2O_3 [54]. The density measurements on l-Er_2O_3 were carried out using an electrostatic levitation furnace at the International Space Station [69] because the measurement of density data for liquid at extremely high temperatures on the ground is impossible (the details of the density measurements are introduced in Chap. 2). The X-ray total structure factors $S(Q)$ of l-Er_2O_3 (2923 K) [54], l-SiO_2 (2373 K) [70], l-Al_2O_3 (2400 K) [52], and l-ZrO_2 (3073 K) [53] are compared in Fig. 4.8a. Note that scaling to the magnitude of the scattering vector Q

is applied by multiplying Q by $r_{A–X}$. A prominent FSDP is found only in the $S(Q)$ of l-SiO_2 at $Qr_{A–X} = 2.6$, because l-SiO_2 is a typical glass-forming liquid. On the other hand, a PP appears in the $S(Q)$ of both l-Er_2O_3 and l-ZrO_2 at $Qr_{A–X} \sim 4.5$. On the other hand, the $S(Q)$ of l-Al_2O_3 shows a very small peak between the positions of FSDP and PP, indicating that l-Al_2O_3 possesses an intermediate structure [54] between l-SiO_2 and l-Er_2O_3/l-ZrO_2. Because the PP is an indicator of oxygen packing in ND data due to the large O–O weighting factor for neutrons (see Chap. 2), no PP is observed in the X-ray $S(Q)$ of l-SiO_2 and l-Al_2O_3. On the other hand, the origin of the PP in the X-ray $S(Q)$ of l-Er_2O_3 and l-ZrO_2 is attributed to the packing of heavy elements, since X-rays are sensitive to them. Figure 4.8b shows the X-ray total correlation functions $T(r)$ of l-Er_2O_3 [54], l-SiO_2 [70], l-Al_2O_3 [52], and l-ZrO_2 [53]. The first correlation peak, observed at 2.2 Å in the $T(r)$ of l-Er_2O_3, is assigned to the Er–O correlation, and a tail of the first peak to ~3 Å suggests that the ErO_n polyhedral unit is distorted. The second peak observed at 3.7 Å is assigned mostly to the Er–Er correlation, which shows the distance between centers of ErO_n polyhedra. The contribution of O–O correlation is almost inappreciable because of its small weighting factor for X-rays. Both the Er–O distance of 2.2 Å and the Zr–O distance of 2.1 Å are longer than those of Si–O (~1.63 Å) at 2373 K and Al–O (~1.78 Å) at 2400 K owing to substantial differences between the radii of the cations. The longer cation–oxygen atomic distance in l-Er_2O_3 and l-ZrO_2 indicates that the oxygen coordination number around a cation is greater than 4. This is because the Er–O distance (2.2 Å) and Zr–O distance (2.1 Å) are close to the sum of the ionic radii (sixfold zirconium, 0.72 Å; sixfold erbium, 0.89 Å; oxygen:1.35 Å) [71]. Therefore, the structures of l-Er_2O_3 and l-ZrO_2 comprise the interconnected polyhedral units with high cation–oxygen coordination numbers and are very different from those of l-SiO_2 and l-Al_2O_3. This behavior of coordination numbers is in line with the absence of the FSDP, which appears owing to a sparse distribution of planes in polyhedra in typical glass-forming oxide glasses in XRD data (Fig. 4.8a). Indeed, there is no such structural ordering manifested by FSDPs in l-Er_2O_3 and l-ZrO_2 owing to their very densely packed structure. Koyama et al. also performed a combination of RMC-MD simulations and revealed that the structure of l-Er_2O_3 consists of linearly arranged distorted OEr_4 tetraclusters, giving rise to a long periodicity, which is the origin of the extraordinarily sharp PP in the X-ray $S(Q)$. Moreover, persistent homology [72] analysis shows that the homology of l-Er_2O_3 is similar to that of the crystalline phase [73]. Additional density functional (DF)-MD simulations suggest that the viscosity of this liquid is very low indicating that l-Er_2O_3 is an extremely fragile liquid [54].

4.9 X-Ray Diffraction Measurements Under High Pressure

Diffraction patterns from non-crystalline materials such as glasses and liquids are broad because their structural periodicity does not continue over long distances. Experimentalists generally need diffraction data with high S/N ratio in order to obtain reliable structural information on glasses and liquids. In situ XRD measurements of

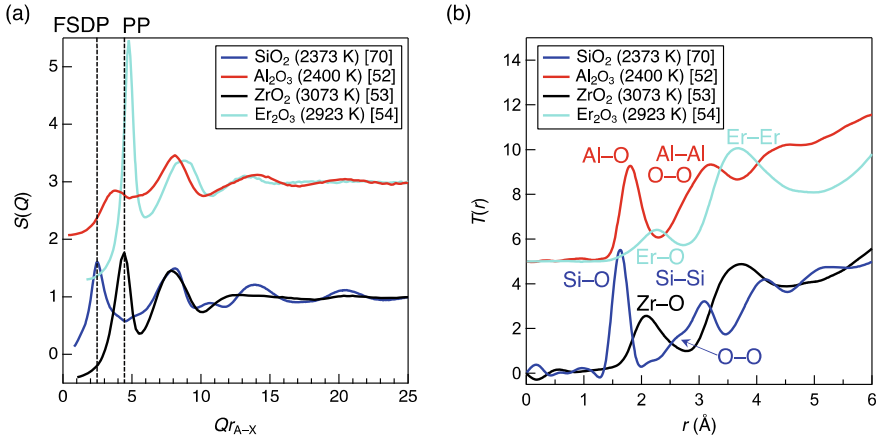

Fig. 4.8 **a** X-ray total structure factors $S(Q)$ and **b** total correlation functions $T(r)$ of l-SiO_2 (2373 K) [70], l-Al_2O_3 (2400 K) [52], l-ZrO_2 (3073 K) [53], and l-Er_2O_3 (2923 K) [54]. Scaling to the magnitude of scattering vector Q is applied by multiplying Q by $r_{A–X}$ (first interatomic distance observed in total correlation functions). Reproduced from Ref. [54] (CC BY 4.0)

glass under high pressure are different from those at ambient pressure as follows: the amount of a sample is limited, the effect of scattering from other materials (e.g., anvils, gaskets, and pressure media) is inevitable and significant, and the aperture angle, or 2θ, is limited because the measurements must be conducted using pressure-generating apparatuses. Most of high-pressure in situ XRD measurements of glasses and liquids are performed using a diamond anvil cell (DAC) apparatus or a large volume press (LVP) in combination with synchrotron X-rays. The methods of XRD measurements with these two types of apparatuses are presented below.

A DAC is a very simple apparatus and mainly consists of two jewel-like-shaped diamonds (e.g. brilliant cut, drukker cut), called diamond anvils (Fig. 4.9). Their tips are cut off and flattened, and they face each other to compress a sample uniaxially. Samples are generally held in a hole drilled in a plate (generally metallic) called a gasket. This apparatus is small, easy to handle, and really compatible with XRD measurements using synchrotron radiation because the volume of samples becomes quite small (10–100 μm size). A DAC can generate pressures up to 400 GPa or higher at room temperature. Temperature conditions of several thousand kelvins can be realized simultaneously by focusing a near-infrared or infrared laser beam and irradiating it through the anvil to the sample. For example, XRD measurements of silicate liquids at 60 GPa/3000 K have been reported [74].

Usually, XRD measurements with a DAC are conducted using monochromatic X-rays, which are injected from a direction parallel to the compression axis, and scattered X-rays are recorded by a two-dimensional detector installed downstream (Fig. 4.9a). In this case, the use of single-crystal diamond anvils minimizes diffraction from the diamonds unless diffraction conditions are not fulfilled, which is very convenient, especially in experiments on powder crystalline materials. However, the

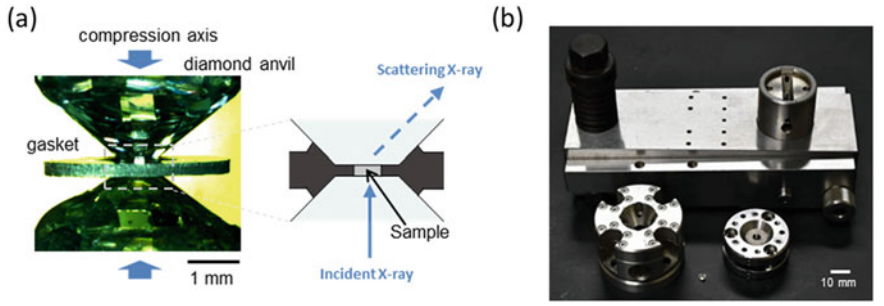

Fig. 4.9 Diamond anvil cell (DAC) apparatus. **a** Diamond anvils and gaskets. **b** Various forms of DAC apparatus for loading

thickness of the sample along the X-ray path is typically less than 100 μm, whereas that of two diamond anvils together are typically 3–4 mm; thus, the Compton scattering from diamond anvils is much stronger than that from the sample. In addition, when using high-energy X-rays (e.g. >30 keV), it is impossible to avoid all diffraction conditions of diamond anvils, and it is often difficult to remove these diffraction spots, especially for weak oscillations from non-crystalline materials in the high-Q region. The signal from diamond anvils becomes a serious noise mainly in the high-Q region, especially for non-crystalline materials composed of light elements such as silicates. Therefore, it is crucial to remove these noises appropriately to obtain reasonable data. In addition, to obtain an accurate pair distribution function $g(r)$, it is desirable to obtain a total structure factor $S(Q)$ up to a high-Q region, preferably up to about $Q = 15$ Å^{-1}. In order to maintain the strength of the base seats supporting the diamonds (e.g., tungsten carbide is commonly used in room-temperature experiments), an aperture for diffraction is usually set to about 60° (i.e., $2\theta = 30°$). In this case, the 30 keV X-rays, which are commonly used in DAC experiments, will result in as low as $Q = 7.9$ Å^{-1} at $2\theta = 30°$.

To remove Compton scattering from diamonds, the most commonly used method is to measure scattering profiles from an empty DAC without a sample before and/or after the experiments and subtract them from the sample profiles as background. Even then, accurate subtraction is not always easy. A perforated diamond anvil, which is an anvil curved along the X-ray path, can also work for reducing diamond Compton scattering [75]. For insufficient aperture angle problems, some attempts to overcome them have been reported by using monochromatic X-rays with high energy (e.g., 100 keV) [76] and by developing a high-aperture-type DAC with machining anvils and base seats to support loads effectively [77]. Measurements up to high-Q region can be also achieved by reducing and subtracting the Compton scattering from diamonds with the energy dispersive method [78], which is often used in experiments with large presses as described below. However, when using either method, the intensity of coherent scatterings rapidly decreases at high Q, and accurate high-pressure in situ measurement of $S(Q)$ at above $Q = 10$ Å^{-1} is very difficult, especially at pressures higher than 100 GPa because the sample becomes very small. Furthermore, it is

difficult to obtain detailed structural information such as interatomic distances and coordination numbers from $g(r)$ alone owing to the overlapping of peaks from many elements. Recently, however, attempts have been made to combine measurements in a limited Q region with first principles and/or classical molecular dynamics (MD) calculations to investigate the details of structural changes [41, 42, 79, 80].

Large volume press (LVP) is an apparatus to compress a sample cell assembly consisting of a sample, pressure-transmitting medium, sample capsule, and heaters to achieve high pressure and high temperature using multiple anvils with a hydraulic press. The anvils are mainly made of tungsten carbide. The sample size is on millimeter order. LVP has advantages in large-sample synthesis, experiments, and precise and stable temperature and pressure control. There are various types of LVP apparatus depending on the pressurization method. Mainly two types of LVP are used for XRD experiments because it is necessary to secure the path of the incident and scattered X-rays. One is the DIA type, which is a cubic-anvil apparatus that compresses a cubic sample cell with six anvils, and the other is the Kawai-type multi-anvil apparatus, which pressurizes an octahedral sample cell assembly with eight second-stage anvils with one corner of the cube cut off using the DIA type as the first-stage anvil (Fig. 4.10). The upper limit of the generated pressure is determined by the strength of the anvil. At high temperatures, the generated pressure becomes lower than that at room temperature because the pressure-transmitting medium softens. For example, pressures of 27 GPa/3000 K [81] and 44 GPa/2000 K [82] with tungsten carbide anvils and over 100 GPa [83] with sintered diamonds have been reported. The Paris–Edinburgh (PE)-type LVP, which was developed to increase the sample volume for high-pressure neutron scattering experiments has also been used for XRD of liquids [84] and glasses [85] (Fig. 4.11). In situ ND measurements of glass under high pressure have also been reported [42, 80, 86]. The sample is uniaxially compressed by two conical anvils using a compact hydraulic press. These conical anvils have a cup in the center to increase the sample size up to a few mm. The usual upper limit of pressure attainable with a PE press is less than 10 GPa. Measurements up to above 100 GPa in sub-mm sizes have also been realized by inserting diamond anvils inside the PE press [85].

In XRD measurements using a Kawai-type apparatus, white X-rays are collimated to about 10–100 μm by a slit usually composed of tungsten carbide or another slit and irradiated to the sample through the gap between the first- and second-stage anvils. Scattered X-rays passing through the anvil gap on the other sides are again collimated by a narrow slit and detected at multiple diffraction angles with a Ge solid-state detector held on a goniometer rotating vertically/horizontally. This method is called the energy-dispersive XRD and is most commonly used for LVP experiments (e.g., Ref. [88]). This technique has the advantage that both incident and scattered X-rays are collimated by slits, thereby eliminating scattered X-rays from regions other than the sample. The lower limit of X-ray energy is about 30 keV owing to absorption by the sample cell and the upper limit is about 60–80 keV, depending on the X-ray energy distribution at the beamline. Due to geometrical constraints, goniometers often have a range of motion up to $2\theta = 20$–$25°$, so ideally, structural information up to $Q \sim 20$ Å^{-1} would be expected. However, the intensity of coherent

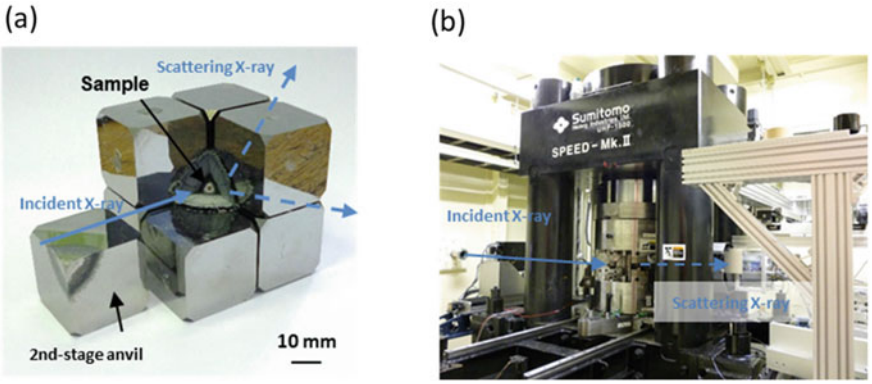

Fig. 4.10 Example of LVP apparatus. **a** picture of inner parts of a Kawai-type multianvil apparatus, provided by Kawazoe [87]. **b** Picture of a multianvil press SPPED-Mk. II at SPring-8 BL04B2, Japan Synchrotron Radiation Research Institute (JASRI)

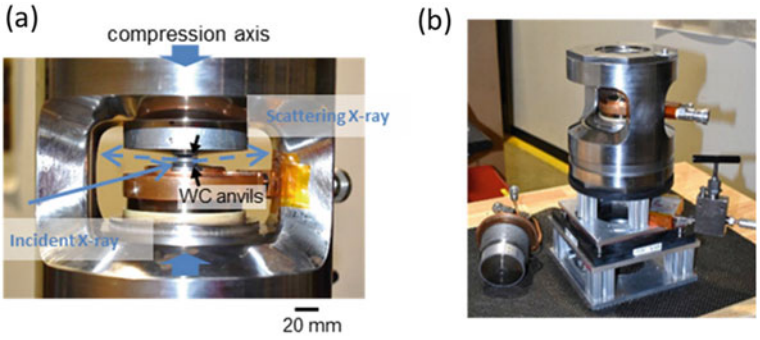

Fig. 4.11 PE type LVP. **a** WC anvils and gaskets. **b** Picture of a PE press used at the sector 16-BM-B beamline, High Pressure Collaborative Access Team (HPCAT) at the Advanced Photon Source, Argonne National Laboratory [84], provided by T. Yu

scattering decreases rapidly at high Q and measurements are not actually easy even for $Q > 15$ Å^{-1}. Since a PE press is a uniaxial compression-type apparatus, it can realize observations at much wider angles than a multianvil apparatus in the direction perpendicular to the compression axis. For example, precise $S(Q)$ up to $Q = 22$ Å^{-1} at 5.3 GPa and 1873 K for liquid $NaAlSi_3O_8$ by energy dispersive XRD in the range of $2\theta = 3$–$37°$ has been reported [84].

4.10 Diffraction Measurements of Silica and Silicate Glasses Under High Pressure

Structural measurements by XRD and ND of glasses and liquids under high pressures are of particular interest from the perspectives of condensed matter physics, materials science, and Earth and planetary science. In recent years, the idea of "polyamorphism", which means that there are phase transitions in non-crystalline materials as well as crystalline materials, has been widely accepted. It is considered that liquids and glasses have phases that are thermodynamically stable or metastable but with low potential energy and separated by energy barriers. High-pressure synthesized glasses sometimes exhibit desirable properties that cannot be obtained at ambient pressure, and are of interest from the viewpoint of synthesizing new glass materials. From the viewpoint of Earth and planetary science, determination of physical and chemical properties of silicate liquids (magmas) or metallic liquids (mainly iron-based), which now exist or have existed in the interior of the Earth and other planets, is necessary for clarifying what is happening or has happened in the planets. In this section, some of the works on high-pressure in situ diffraction experiments of silica and silicate glass will be presented.

Silica (SiO_2) glass is the most typical glass with a three-dimensional network structure with SiO_4 tetrahedra as the basic unit at ambient pressure. It is definitely one of the most well-studied glasses in the field of high-pressure science. Pressure induces significant changes in the short- and intermediate-range structure of SiO_2 glass: the permanent densification at around 10 GPa, the coordination number change from SiO_4 tetrahedra to SiO_6 octahedra at 20–40 GPa, and the change to over sixfold-coordinated structures occurring at above 100 GPa are noteworthy. The first high-pressure in situ XRD measurement of SiO_2 glass was reported in 1992 [89]. At that time, it was difficult to measure $S(Q)$ in a sufficient Q region to obtain an accurate $g(r)$. Technical developments in high-pressure and synchrotron techniques have led to XRD at high temperatures [90], XRD up to 100 GPa [91], ND up to 18 GPa [42], and XRD above 100 GPa [41, 92, 93], revealing details of pressure-induced structural changes in SiO_2 glass.

X-ray $S(Q)$ of SiO_2 glass measured up to 100 GPa are shown in Fig. 4.12. The obvious peak at around 1.6–2.5 $Å^{-1}$ is the FSDP. As mentioned in Sect. 4.5, the FSDP is observed owing to the positive contributions of the Si–Si, Si–O, and O–O partial structure factors, and it is considered to reflect the arrangement of voids and/or cages in a SiO_4 tetrahedral network, i.e., the intermediate-range structure. The PP at around 3 $Å^{-1}$ is observed only at a high pressure. This peak is not observed by XRD but clearly observed by ND at ambient pressure, and is considered to reflect the packing of oxygen atoms. With increasing pressure, the PP becomes observable in XRD at about 10 GPa and prominent at above 20 GPa. This behavior is understood in terms of the Si–Si partial structure factor obtained by MD simulation, in which the Si–Si PP increases with increasing pressure [41].

Permanent densification (or densification) [95] is a phenomenon that when glass is subjected to a pressure of about 10 GPa and then recovered, the glass becomes

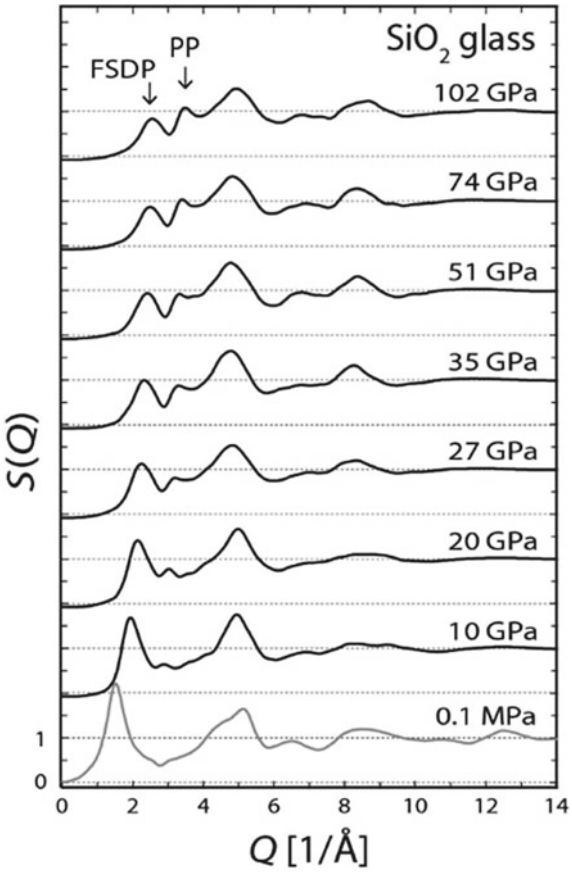

Fig. 4.12 X-ray total structure factors $S(Q)$ of SiO_2 glass under high pressures [91]. The patterns at 0.1 MPa are from [94]

denser than before compression. This phenomenon has been reported for silicate, aluminosilicate, and borate glasses of various compositions, as well as SiO_2 glass. It is also reported for bulk metallic glasses and chalcogenide glasses. In the case of SiO_2 glass, density increases of up to 20–25% have been reported [96, 97]. Densification is attributed to the contraction of voids in the intermediate-range network structure by compression. The simultaneous application of temperature significantly promotes densification, resulting in higher densities at lower pressures [89, 98]. FSDP shifts toward higher Q by the densification in oxide glasses with various compositions. Although PP is sharp and distinct under high pressures, it is not observed in the recovered densified glasses, and the profiles of $S(Q)$ at above 8 $Å^{-1}$ are very similar before and after compression [99, 100]. This finding also supports the hypothesis that densification is caused by the contraction of the intermediate-range structure with little change in the short-range structure.

A change in the short-range structure occurs at above 20 GPa; the coordination number is 5 at 27 GPa and the pattern at this pressure can be explained fairly well by

mixing the patterns at 20 and 35 GPa. On the other hand, the patterns from 35 to 100 GPa are very similar, although the overall pattern gradually shifts toward higher Q owing to compression (Fig. 4.12). $g(r)$ shows that the Si–O distance increases rapidly from 20 to 35 GPa despite compression, and then decreases at above 35 GPa. The coordination number of oxygen to silicon increases from 4 to 6 from 20 to 35 GPa and remains nearly sixfold-coordinated from 35 GPa to least 100 GPa or higher [91], therefore SiO_2 glass may be considered to behave as a "sixfold-coordinated phase" in this pressure range. At ambient pressure, it is considered that almost 100% of the Si is fourfold-coordinated. On the other hand, MD calculations have suggested that only about 75% of Si species are sixfold-coordinated and five- and seven-coordinated species also exist in a "sixfold-coordinated phase" [41]. At higher pressures, the coordination number begins to increase above 100–140 GPa [41, 92, 93]; at 200 GPa, it is suggested by a combination of XRD measurements and MD calculations that the average coordination number becomes 7 with a similar short-range structure to pyrite-type silica crystal [41].

Silicate glasses also have a network structure based on SiO_4 or AlO_4 tetrahedra at ambient pressure, but their network is modified or disconnected by network-modifying cations (e.g., Na, Mg, and Ca). The structure of silicate liquids under high pressure is particularly important from the geophysical viewpoint, but the melting point of silicates is very high (usually >2000 K), and experiments at high temperatures are often much more difficult than those at room temperature. The high-pressure structure of glasses is expected to resemble those of liquids with the same composition, especially in the case of "strong" glass-forming liquids [49]. High-pressure in situ XRD measurements have been carried out for geophysically important compositions such as $MgSiO_3$ [101], Mg_2SiO_4 [102], jadeite ($NaAlSi_2O_6$) [103], basalt (aluminosilicate containing cations such as Mg, Ca, and Fe) [86], as well as aluminum-rich compositions such as anorthite ($CaAl_2Si_2O_8$) and silica-free $CaAl_2O_4$ [79]. ND measurements have also been reported for $MgSiO_3$ and $CaSiO_3$ [80] and basalt [86] glasses. Owing to the technical difficulties in obtaining high-Q data, the peaks in $g(r)$ become broader, which makes it almost impossible to assign various atomic pairs corresponding to each peak. In most cases, diffraction data are not sufficient for discussing the detailed structure. This difficulty can be partly compensated with the help of MD calculations, but the results of calculations and experiments do not always agree well. Future improvements in measurements are strongly expected. Note that the description below is not necessarily based on the results of experiments but includes many predictions based on MD calculations.

FSDP is observed for all compositions and located at around 2 $Å^{-1}$ at ambient pressure, which is higher than that in SiO_2 glass, suggesting that the network-modifying cations cleave the network and reduce voids. PP is not observed in the XRD patterns at ambient pressure for all compositions but begins to be observed at pressures above 5–10 GPa, and becomes more prominent with increasing pressure. An irreversible FSDP shift (densification) has been reported for $MgSiO_3$, $CaSiO_3$, jadeite, and basalt glasses, whereas the XRD pattern is considered to be reversible for Mg_2SiO_4. This may be due to the fact that the network structure of Mg_2SiO_4 at ambient pressure is dominated by MgO_x, not by SiO_4 [104]. The FSDP of jadeite glass is not

so prominent at ambient pressure but becomes sharper with increasing pressure and subsequent temperature increase. The recovered FSDP is sharp and clear. Since crystalline jadeite is thermodynamically stable only at high pressures, the drastic change in the FSDP suggests that liquid (and glass) structures at ambient pressure and high pressure may be very different. The coordination number of Si is suggested to remain four below 20 GPa as in SiO_2 glass because the Si–O bond length shows almost no change for $MgSiO_3$, $CaSiO_3$, Mg_2SiO_4, anorthite, and basalt. However, there is a study suggesting that the Si–O bond length significantly increases and the coordination number begins to increase already at 10 GPa [101]. NMR measurements for recovered samples indicate that Al consumes non-bridging oxygen at lower pressures than Si to increase its coordination number [105]. The coordination number of Al in both $CaAl_2Si_2O_8$ and $CaAl_2O_4$ starts to increase from 0 GPa and sixfold-coordinated species become dominant at 20 GPa. The approximate average coordination numbers of network-modifying cations for glasses at ambient pressure are reported as follows: 4.5 for $MgSiO_3$ [106], 5 for Mg_2SiO_4 with a mixture of 4, 5, and 6 [104], 6 for $CaSiO_3$ [80], and 6.5 for anorthite [79]. The coordination number of Mg and Ca in crystalline phases with the same compositions is 6. Therefore all compositions except $CaSiO_3$ seem to have different coordination states in crystals and glasses. The coordination number will increase with pressure to 6 for $MgSiO_3$, 7.5 for $CaSiO_3$, and 9 for anorthite at about 20 GPa. High-pressure in situ diffraction measurements of silicate glass have been limited, and it is not fully understood how structural changes occur under pressure; however, such information will be of great interest for the development of new materials.

4.11 Permanently Densified SiO_2 Glass Recovered After Hot Compression

As described in the previous section, the FSDP in diffraction data for SiO_2 glass shifts toward higher Q and diminishes under high pressure at room temperature (cold compression) as shown in Fig. 4.12. Although this trend observed under cold compression has been understood as a general trend for the behavior of FSDP under high pressure, Onodera et al. reported the unusual behavior of the FSDP in XRD data for SiO_2 glass recovered after hot compression. They recovered densified SiO_2 glasses after hot compression at a pressure of 7.7 GPa and temperatures up to 1473 K, and probed the glass structure by a combination of diffraction measurements and structure modeling [100]. Figure 4.13a shows X-ray $S(Q)$ for hot-compressed SiO_2 glasses. The evolution of FSDP at 7.7 GPa is observed at a temperature higher than 673 K; thus, the sharpness of the FSDP is decreased with increasing a temperature up to 673 K. The density of the hot-compressed SiO_2 glasses also changes in behavior at a temperature higher than 673 K. These results indicate the transformation from a low- to high-density amorphous phase in SiO_2 glass. Onodera et al. prepared a glass

with the same density as the hot-compressed glass (1473 K/7.7 GPa) by cold compression at RT/20 GPa. Figure 4.13b shows X-ray $S(Q)$ for two densified glasses with the same high density (hot-compressed glass, 2.72 g/cm^3; cold-compressed glass, 2.71 g/cm^3). The position of the FSDP is almost the same corresponding to the same density, whereas the sharpness of the FSDP shows a significant difference between the two glasses. The Si–O coordination number obtained from the corresponding $T(r)$ functions is four in each densified glass, indicating that the structure of the densified glasses comprises a network of corner-sharing tetrahedral SiO_4 motifs. The coherence length describing the intermediate-range ordering based on these motifs, given by $2\pi/\Delta Q_{FSDP}$, reaches 12.7 Å for 1473 K/7.7 GPa. On the other hand, the coherence length is 7.9 Å for RT/20 GPa. Therefore, although the densities of 1473 K/7.7 GPa and RT/20 GPa glasses are comparable, their structures are markedly different, with a coherent length for 1473 K/7.7 GPa that is ~61% longer than that for RT/20 GPa. In addition, hot-compressed glasses were stable for at least 1.5 years at ambient conditions, whereas cold-compressed glass showed a reduction in density of 2.8% after 1.5 years, suggesting that permanently densified SiO_2 glasses can be synthesized by hot compression. As mentioned above, the glass structure can be controlled by controlling the processing conditions such as temperature and pressure. The densified SiO_2 glass has attracted much attention as a candidate core material for optical fibers capable of reducing loss (see Chap. 15). The knowledge of the glass structure obtained by diffraction measurements may therefore be helpful for the design of new glassy materials.

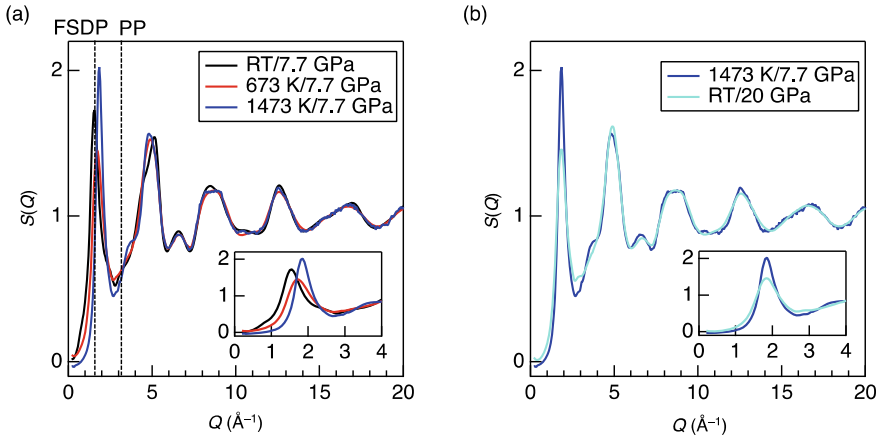

Fig. 4.13 **a** X-ray total structure factors $S(Q)$ of SiO_2 glasses recovered after hot compression. **b** X-ray total structure factors $S(Q)$ of hot- and cold-compressed SiO_2 glasses

4.12 Summary

This chapter described a brief introduction to the pair distribution function (PDF) analysis by X-ray and neutron diffraction measurements of disordered materials. Although solving the structure of disordered materials such as glasses, liquids, and amorphous materials is difficult owing to the lack of long-range periodicity, the PDF provides real-space structural information, such as interatomic distance and coordination number. Moreover, the complementary use of X-rays and neutrons enables us to analyze disordered structures more precisely by utilizing the contrast between X-ray form factors and neutron coherent scattering length. Attempts to understand the origin of diffraction peaks observed in diffraction patterns of typical disordered materials are made. The first sharp diffraction peak (FSDP) appears as the result of a sparse distribution of planes in polyhedra. The principal peak (PP) is a signature of the formation of chemical bond and reflects inter-polyhedral correlations on a short-length scale compared with FSDP. The extraordinarily sharp PP observed in neutron diffraction data for Al_2O_3 glass fabricated by the electro-chemical anodization of Al metal indicates the formation of a densely oxygen-packed structure with a small cavity volume that is completely outside of Zachariasen's glass-forming concept. The dedicated diffractometer for accurate diffraction measurement on levitated liquid under high temperatures is available at SPring-8. The structure of a representative nonglass-forming liquid, Er_2O_3, was successfully discovered by applying an aerodynamic levitation technique and high-energy X-rays. Experimental methods of X-ray diffraction measurements for disordered materials under high pressures are introduced together with the results of diffraction measurements of silica and silicate glasses under high pressures. In particular, the unusual behavior of the FSDP was found in the X-ray diffraction data for permanently densified SiO_2 glass synthesized by hot compression at a pressure of 7.7 GPa and a temperature of 1473 K. The advent of synchrotron and neutron facilities led to the accurate measurement of diffraction of disordered materials from ambient to extreme (high pressure and high temperature) conditions.

Acknowledgements This work was supported by a JSPS Grant-in-Aid for Transformative Research Areas (A) "Hyper-Ordered Structures Science": Grants No. 20H05878, No. 20H05879 and No. 20H05881. The authors greatly appreciate Prof. Hidenori Goto, Prof. Takayoshi Yokoya, Mr. Mitsuki Ikeda, Dr. Ritsuko Eguchi, and Ms. Risa Kawamoto for their valuable suggestions and assistance in completing this section.

References

1. Fisher HE, Barnes HE, Salmon PS (2006) Rep Prog Phys 69:233
2. Kohara S, Salmon PS (2016) Adv Phys: X 1:640
3. Lorch E (1969) J Phys C Solid State 2:229
4. Kohara S, Ohara K, Tajiri H, Song C, Sakata O, Usuki T, Benino Y, Mizuno A, Masuno A, Okada JT, Ishikawa T, Hosokawa S (2016) Z Phys Chem 230:339

5. Hannon AC, Howells WS, Soper AK (1990) Inst Phys Conf Ser 107:193
6. Keen DA (2001) J Appl Crystallogr 34:172
7. Ohara K, Murakami M, Onodera Y, Kohara S (2021) J Phys Condens Matter 33:383001
8. Sutter J, Chater P, Hillman MR, Keeble DS, Tucker MG, Wilhelm H (2016) AIP Conf Proc 1741:040005
9. Benmore CJ (2012) ISRN Mater Sci 2012:852905
10. Fischer HE, Cuello GJ, Palleau P, Feltin D, Barnes AC, Badyal YS, Simonson JM (2002) Appl Phys A 74:S160
11. Neuefeind J, Feygenson M, Carruth J, Hoffmann R, Chipley KK (2012) Nucl Instrum Methods Phys Res B 287:68
12. Bowron DT, Soper AK, Jones K, Ansell S, Birch S, Norris J, Perrott L, Riedel D, Rhodes NJ, Wakefield SR, Botti A, Ricci M-A, Grazzi F, Zoppi M (2010) Rev Sci Instrum 81:033905
13. Otomo T, Suzuya K, Misawa M, Kaneko N, Ohshita H, Ikeda K, Tsubota M, Seya T, Fukunaga T, Itoh K, Sugiyama M, Mori K, Kameda Y, Yamaguchi T, Yoshida K, Maruyama K, Kawakita Y, Shamoto S, Kodama K, Takata S, Satoh S, Muto S, Ino T, Shimizu HM, Kamiyama T, Ikeda S, Itoh S, Yasu Y, Nakayoshi K, Sendai H, Uno S, Tanaka M, Ueno K (2011) KENS Rep 17:27
14. Kohara S, Suzuya K (2003) Nucl Instr Methods Phys Res B 199:23
15. Hannon AC (2005) Nucl Instrum Methods Phys Res A 551:88
16. Salmon PS, Martin RA, Mason PE, Cuello GJ (2005) Nature 435:75
17. Price DL, Moss SC, Reijers R, Saboungi M-L, Susman S (1988) J Phys C Solid State 21:L1069
18. Salmon PS (2018) Magma under pressure: advances in high-pressure experiments on structure and properties of melts. Elsevier, Amsterdam
19. Onodera Y, Kohara S, Tahara S, Masuno A, Inoue H, Shiga M, Hirata A, Tsuchiya K, Hiraoka Y, Obayashi I, Ohara K, Mizuno A, Sakata O (2019) J Ceram Soc Jpn 127:853
20. Onodera Y, Takimoto Y, Hijiya H, Taniguchi T, Urata S, Inaba S, Fujita S, Obayashi I, Hiraoka Y, Kohara S (2019) NPG Asia Mater 11:75
21. Wright AC, Leadbetter AJ (1976) Phys Chem Glasses 17:122
22. Phillips JC (1981) Non-Cryst J Solids 43:4337
23. Zachariasen WH (1932) J Am Chem Soc 54:3841
24. Mei Q, Benmore CJ, Sen S, Sharma R, Yargar J (2008) Phys Rev B 78:144204
25. Laaziri K, Kycia S, Roorda S, Chicoine M, Robertson JL, Wang J, Moss SC (1999) Phys Rev Lett 82:3460
26. Zeidler A, Salmon PS, Martin RA, Usuki T, Mason PE, Cuello GJ, Kohara S, Fischer HE (2010) Phys Rev B 82:104208
27. Bychkov E, Benmore CJ, Price DL (2005) Phys Rev B 72:172107
28. Bytchkov A, Cuello GJ, Kohara S, Benmore CJ, Price DL, Bychkov E (2013) Phys Chem Chem Phys 15:8487
29. Hannon AC, Di Martino D, Santos LF, Almeida RM (2007) J Phys Chem B 111:3342
30. Morita H, Kohara S, Usuki T (2009) J Mol Liq 147:182
31. Katayama Y, Mizutani T, Utsumi W, Shimomura O, Yamakata M, Funakoshi K (2000) Nature 403:170
32. Salmon PS, Barnes AC, Martin RA, Cuello GJ (2006) Phys Rev Lett 96:235502
33. Zeidler A, Salmon PS, Skinner LB (2011) Proc Natl Acad Sci USA 108:14780
34. Reijers HTJ, Saboungi M-L, Price DL, Richardson JW Jr, Volin KJ (1989) Phys Rev B 40:6018
35. Stolz M, Winter R, Howells WS, McGreevy RL (1990) J Phys: Condens Matter 7:5733
36. Toukan K, Reijers HTJ, Loong C-K, Price DL, Saboungi M-L (1990) Phys Rev B 41:11739
37. Pothoczki Sz, Temleitner L, Pusztai L (2015) Chem Rev 115:13308
38. Hannon AC, Grimley DI, Hulme RA, Wright AC, Sinclair RN (1994) Non-Cryst J Solids 197:299
39. Clare AG, Wright AC, Sinclair RN, Galeener FL, Geissberger AE (1989) Non-Cryst J Solids 111:123
40. Zeidler A, Salmon PS (2016) Phys Rev B 93:214204

41. Murakami M, Kohara S, Kitamura N, Akola J, Inoue H, Hirata A, Hiraoka Y, Onodera Y, Obayashi I, Kalikka J, Hirao N, Musso T, Foster AS, Idemoto Y, Sakata O, Ohishi Y (2019) Phys Rev B 99:045153
42. Zeidler A, Wezka K, Rowlands RF, Whittaker DAJ, Salmon PS, Polidori A, Drewitt JWE, Klotz S, Fischer HE, Wilding MC, Bull CL, Tucker MG, Wilson M (2014) Phys Rev Lett 112:135501
43. Misawa M (1989) J Chem Phys 91:5648
44. Pothoczki Sz, Temleitner L, Jóvári P, Kohara S, Pusztai L (2009) J Chem Phys 130:064503
45. Bernal JD (1959) Nature 183:141
46. Sadoc JF, Dixmier J, Guinier A (1973) Non-Cryst J Solids 12:46
47. Cargill GS III, Kirkpatrick S (1976) AIP Conf Proc 31:339
48. Kohara S, Shiga M, Onodera Y, Masai H, Hirata A, Murakami M, Morishita T, Kimura K, Hayashi K (2021) Sci Rep 11:22180
49. Skinner LB, Benmore CJ, Weber JKR, Wilding MC, Tumber SK, Parise JB (2013) Phys Chem Chem Phys 15:8566
50. Sun K-H (1947) J Am Ceram Soc 30:277
51. Hashimoto H, Onodera Y, Tahara S, Kohara S, Yazawa K, Segawa H, Murakami M, Ohara K (2022) Sci Rep 12:516
52. Skinner LB, Barnes AC, Salmon PS, Hennet L, Fischer HE, Benmore CJ, Kohara S, Weber JKR, Bytchkov A, Wilding MC, Parise JB, Farmer TO, Pozdnyakova I, Tumber SK, Ohara K (2013) Phys Rev B 87:024201
53. Kohara S, Akola J, Patrikeev L, Ropo M, Ohara K, Itou M, Fujiwara A, Yahiro J, Okada JT, Ishikawa T, Mizuno A, Masuno A, Watanabe Y, Usuki T (2014) Nat Commun 5:5892
54. Koyama C, Tahara S, Kohara S, Onodera Y, Småbråten DR, Selbach SM, Akola J, Ishikawa T, Masuno A, Mizuno A, Okada JT, Watanabe Y, Nakata Y, Ohara K, Tamaru H, Oda H, Obayashi I, Hiraoka Y, Sakata O (2020) NPG Asia Mater 12:43
55. Price DL (2010) High-temperature levitated materials. Cambridge University Press, Cambridge
56. Ansell S, Krishnan S, Weber JKR, Felten JJ, Nordine PC, Beno MA, Price DL, Saboungi M-L (1997) Phys Rev Lett 78:464
57. Landron C, Hennet L, Jenkins TE, Greaves GN, Coutures JP, Soper AK (2001) Phys Rev Lett 86:4839
58. Krishnan S, Hennet L, Jahn S, Key TA, Madden PA, Saboungi M-L, Price DL (2005) Chem Mater 17:2662
59. Shi C, Alderman OLG, Merman D, Du J, Neuefeind J, Tamalonis A, Weber JKR, You J, Benmore CJ (2019) Front Mater 6:38
60. Jahn S, Madden PA (2007) Non-Cryst J Solids 353:3500
61. Vashishta P, Kalia RK, Nakano A, Rino JP (2008) J Appl Phys 103:083504
62. Skinner LB, Benmore CJ, Weber JKR, Williamson MA, Tamalonis A, Hebden A, Wiencek T, Alderman OLG, Guthrie M, Leibowitz L, Parise JB (2014) Science 346:984
63. Alderman OLG, Benmore CJ, Weber JKR, Skinner LB, Tamalonis AJ, Sendelbach S, Hebden A, Williamson MA (2018) Sci Rep 8:2434
64. Skinner LB, Benmore CJ, Weber JKR, Du J, Neuefeind J, Tumber SK, Parise JB (2014) Phys Rev Lett 112:157801
65. Hong QJ, Ushakov SV, Kapush D, Benmore CJ, Weber JKR, Walle A, Navrotsky A (2018) Sci Rep 8:14962
66. Ohara K, Onodera Y, Kohara S, Koyama C, Masuno A, Mizuno A, Okada JT, Tahara S, Watanabe Y, Oda H, Nakata Y, Tamaru H, Ishikawa T, Sakata O (2020) Int J Microgravity Sci Appl 37:370202
67. Kohara S, Ohara K, Ishikawa T, Tamaru H, Weber JKR (2018) Quantum Beam Sci 2:1
68. Angell CA (1995) Science 267:1924
69. Tamaru H, Koyama C, Saruwatari H, Nakamura Y, Ishikawa T, Takada T (2018) Microgravity Sci Technol 30:643
70. Mei Q, Benmore CJ, Weber JKR (2007) Phys Rev Lett 98:057802

71. Shannon RD, Prewitt CT (1969) Acta Cryst B 25:925
72. Hiraoka Y, Nakamura T, Hirata A, Esscolar EG, Matsue K, Nishiura Y (2016) Proc Natl Acad Sci USA 113:7035
73. Saiki A, Ishizawa N, Mizutani N, Kato M (1985) Yogyo Kyokai Shi 93:649
74. Sanloup C, Drewitt JW, Konopkova Z, Dalladay-Simpson P, Morton DM, Rai N, van Westrenen W, Morgenroth W (2013) Nature 503:104
75. Soignard E, Benmore CJ, Yarger JL (2010) Rev Sci Instrum 81:035110
76. Benmore CJ, Soignard E, Amin SA, Guthrie M, Shastri SD, Lee PL, Yarger JL (2010) Phys Rev B 81:054105
77. Boehler R, De Hantsetters K (2004) High Press Res 24:391
78. Sato T, Funamori N, Kikegawa T (2010) Rev Sci Instrum 81:043906
79. Drewitt JWE, Jahn S, Sanloup C, de Grouchy C, Garbarino G, Hennet L (2015) J Phys: Condens Matter 27:105103
80. Salmon PS, Moody GS, Ishii Y, Pizzey KJ, Polidori A, Salanne M, Zeidler A, Buscemi M, Fischer HE, Bull CL, Klotz S, Weber R, Benmore CJ, MacLeod SG (2019) J Non-Cryst Solids: X 3:100024
81. Kawazoe T, Ohtani E (2006) Phys Chem Miner 33:227
82. Ishii T, Shi L, Huang R, Tsujino N, Druzhbin D, Myhill R, Li Y, Wang L, Yamamoto T, Miyajima N, Kawazoe T, Nishiyama N, Higo Y, Tange Y, Katsura T (2016) Rev Sci Instrum 87:024501
83. Yamazaki D, Ito E, Yoshino T, Tsujino N, Yoneda A, Guo X, Xu F, Higo Y, Funakoshi K (2014) Phys Earth Planet Inter 228:262
84. Yamada A, Wang Y, Inoue T, Yang W, Park C, Yu T, Shen G (2011) Rev Sci Instrum 82:015103
85. Kono Y, Kenney-Benson C, Ikuta D, Shibazaki Y, Wang Y, Shen G (2016) Proc Natl Acad Sci USA 113:3436
86. Ohashi T, Sakamaki T, Funakoshi K, Hattori T, Hisano N, Abe J, Suzuki A (2022) Am Min 107:325
87. Kawazoe T. https://home.hiroshima-u.ac.jp/kawazoe/html/Kawazoe04-Method-EN.html
88. Utsumi W, Funakoshi K, Urakawa S, Yamakata M, Tsuji K, Konishi H, Shimomura O (1998) Rev High Press Sci Technol 7:1484
89. Meade C, Hemley RJ, Mao HK (1992) Phys Rev Lett 69:1387
90. Inamura Y, Katayama Y, Utsumi W, Funakoshi K (2004) Phys Rev Lett 93:015501
91. Sato T, Funamori N (2010) Phys Rev B 82:184102
92. Prescher C, Prakapenka VB, Stefanski J, Jahn S, Skinner LB, Wang Y (2017) Proc Natl Acad Sci USA 114:10041
93. Kono Y, Shu Y, Kenney-Benson C, Wang Y, Shen G (2020) Phys Rev Lett 125:205701
94. Funamori N, Yamamoto S, Yagi T, Kikegawa T (2004) J Geophys Res 109:B03203
95. Bridgman PW, Šimon I (1953) J Appl Phys 24:405
96. Rouxel T, Ji H, Hammouda T, Moréac A (2008) Phys Rev Lett 100:225501
97. Wakabayashi D, Funamori N, Sato T, Taniguchi T (2011) Phys Rev B 84:144103
98. Arndt J, Stoffler D (1969) Phys Chem Glasses 10:117
99. Inamura Y, Arai M, Nakamura M, Otomo T, Kitamura N, Bennington SM, Hannon AC, Buchenau U (2001) Non-Cryst J Solids 293–295:389
100. Onodera Y, Kohara S, Salmon PS, Hirata A, Nishiyama N, Kitani S, Zeidler A, Shiga M, Masuno A, Inoue H, Tahara S, Polidori A, Fischer HE, Mori T, Kojima S, Kawaji H, Kolesnikov AI, Stone MB, Tucker MG, McDonnell MT, Hannon AC, Hiraoka Y, Obayashi I, Nakamura T, Akola J, Fujii Y, Ohara K, Taniguchi Y, Sakata O (2020) NPG Asia Mater 12:85
101. Kono Y, Shibazaki Y, Kenney-Benson C, Wang Y, Shen G (2018) Proc Natl Acad Sci USA 115:1742
102. Benmore CJ, Soignard E, Guthrie M, Amin SA, Weber JKR, McKiernan K, Wilding MC, Yarger JL (2011) Non-Cryst J Solids 357:2632
103. Sakamaki T, Wang Y, Park C, Yu T, Shen G (2014) Phys Earth Planet Inter 228:281

104. Kohara S, Suzuya K, Takeuchi K, Loong CK, Grimsditch M, Weber JKR, Tangeman JA, Key TS (2004) Science 303:1649
105. Lee SK, Cody GD, Fei Y, Mysen BO (2004) Geochim Cosmochim Acta 68:4189
106. Wilding MC, Benmore CJ, Tangeman JA, Sampath S (2004) Chem Geol 213:281